

Spectroscopy of blue supergiants in the spiral galaxy NGC 300¹

Fabio Bresolin²

Institute for Astronomy, 2680 Woodlawn Drive, Honolulu HI 96822

bresolin@ifa.hawaii.edu

Wolfgang Gieren

Universidad de Concepción, Departamento de Física, Casilla 160-C, Concepción, Chile

wgieren@coma.cfm.udec.cl

Rolf-Peter Kudritzki

Institute for Astronomy, 2680 Woodlawn Drive, Honolulu HI 96822

kud@ifa.hawaii.edu

Grzegorz Pietrzyński³

Universidad de Concepción, Departamento de Física, Casilla 160-C, Concepción, Chile

pietrzyn@hubble.cfm.udec.cl

and

Norbert Przybilla

Universitäts-Sternwarte München, Scheinerstr. 1, 81679, München, Germany

nob@usm.uni-muenchen.de

ABSTRACT

We have obtained VLT low-resolution ($\sim 5 \text{ \AA}$) multi-object spectroscopy in the 4,000-5,000 \AA spectral range of about 70 blue supergiant candidates in the

¹Based on observations obtained at the ESO Very Large Telescope

²On leave from Universitäts-Sternwarte München

³Also affiliated to: Warsaw University Observatory, Al. Ujazdowskie 4, 00-478, Warsaw, Poland

Sculptor Group spiral galaxy NGC 300, selected from previous wide-field photometry. Of the 62 spectroscopically confirmed blue supergiants, with spectral types ranging from late-O to F, 57 have types between early-B and mid-A. We present a detailed spectral catalog containing identification, magnitudes, colors and spectral types.

We employ synthetic spectra calculated from blue supergiant model atmospheres for different metallicities to determine metal abundances for two A0 supergiants of the sample. In agreement with the expectations, the star closer to the galactic center is found to be more metal rich than the object at a larger galactocentric distance. We will employ this technique on the whole supergiant sample to determine the stellar abundance gradient in the disk of NGC 300, together with the internal reddening from a comparison of the observed vs. synthetic colors. This will allow, among other things, an accurate calibration of the effect of metallicity on the Cepheid Period-Luminosity relation.

Using the Balmer $H\beta$ line profile we have estimated the mass-loss rate for one of the brightest A2 supergiants in the sample. Under additional reasonable assumptions we determined the wind momentum of the star and compared it to the value expected from the empirical wind momentum-luminosity relationship (WLR) for A-type supergiants of Kudritzki et al. (1999). Good agreement is obtained. We will derive mass-loss rates and wind momenta for all stars in our sample from the $H\alpha$ line profiles in forthcoming work, and will then thoroughly test the usefulness of the WLR for distance measurement out to about 15 Mpc.

Subject headings: galaxies: individual (NGC 300) — galaxies: stellar content — stars: early-type — stars: winds, outflows

1. Introduction

With the recent advent of 8-10 meter-class telescopes, it has become possible for the first time to carry out quantitative spectroscopic analysis of stellar objects in distant galaxies, opening a new dimension in the study of the stellar content of such galaxies. These studies will not only allow us to investigate the stellar properties, but will also greatly contribute to an understanding of the host galaxies themselves in terms of star formation properties, and their chemical and dynamical evolution. In order to explore this new opportunity, a few years ago we started a program to carry out spectroscopy of blue supergiant stars in a number of nearby galaxies. Blue supergiants are especially well-suited for spectroscopic analysis in the visual part of the spectrum, because at visual wavelengths they belong to the

brightest objects in a galaxy, attaining absolute visual magnitudes as bright as $M_V = -10$, thus pushing the limit for quantitative spectroscopic analysis with 8m-class telescopes out to distance moduli $m - M \simeq 30$. Indeed, we have recently performed the first quantitative spectroscopic analysis of a blue supergiant in the galaxy NGC 3621, at a distance of 6.7 Mpc (Bresolin et al. 2001), more than 100 times the distance to the LMC, and the most distant galaxy in which quantitative stellar spectroscopy has yet been carried out. Other galaxies in which blue supergiants have been studied so far include LMC and SMC (Kudritzki et al. 1989, Lennon et al. 1991, Puls et al. 1996, Venn 1999, de Koter et al. 1998, Dufton et al. 2000), the Inter-Cloud population (Rolleston et al. 1999), M31 (McCarthy et al. 1997, Venn et al. 2000, Smartt et al. 2001), M33 (McCarthy et al. 1995, Monteverde et al. 1997, 2000), and NGC 6822 (Muschielok et al. 1999, Venn et al. 2001), all of them belonging to the Local Group. Going beyond the Local Group, the main scientific driver behind this work is the possibility to derive relatively accurate chemical abundances for these stars together with more accurate estimates of extinction and reddening, even from low resolution ($R \simeq 1000$) optical spectra (Kudritzki 1998), and to use their wind properties which can be determined from the optical spectra to get an independent estimate of the host galaxies distances from the wind momentum-luminosity relationship (WLR, Kudritzki et al. 1999). Indeed, in the latter paper it was shown that there is evidence that the WLR for blue supergiants, once properly calibrated and tested for systematic effects, might yield a standard candle similar in accuracy to Cepheid variables, and reaching out to the distance of the Fornax and Virgo clusters.

Before we can fully use this new instrument of distance measurement, we must thoroughly test its dependence on a number of parameters, most importantly the stellar spectral type and metallicity. An ideal place to carry out such a test, and significantly enhance the number of calibrating objects for the WLR, is the Sculptor Group galaxy NGC 300. At a distance of ~ 2.0 Mpc, as derived from Cepheid variables (Freedman et al. 2001), NGC 300 is close enough to allow quantitative spectroscopy of its blue supergiant population with multiobject spectroscopy at the VLT. Furthermore, NGC 300 shows clear signs of recent massive star forming activity, so a considerable number of blue supergiants can be expected in this galaxy. Indeed, a recent wide-field photometric survey of the galaxy carried out by some of us (Pietrzyński et al. 2001) has identified more than 100 OB associations. This same survey is currently discovering a large number of new Cepheids, and the blue supergiant abundances which we will derive will allow us to determine the abundance gradient in the disk of NGC 300, from which we hope to obtain the first accurate empirical determination of the effect of metallicity on the Cepheid Period-Luminosity (PL) relation, currently only poorly constrained by observations. The effects of reddening will also be investigated, by comparing observed and synthetic colors of individual blue supergiants.

The purpose of this paper is to present our blue supergiant spectroscopy in NGC 300. In Sec. 2 we describe the target selection, and the spectroscopic observations and reductions. In Sec. 3 we present the spectral classification of our targets. In Sec. 4 we discuss some first results regarding metallicities and wind momenta, and our conclusions will be presented in Sec. 5.

2. Blue supergiant selection and spectroscopy

A large set of multi-epoch, broad-band images have been obtained with the Wide Field Imager (WFI) at the ESO/MPI 2.2m telescope on La Silla, as part of a long-term project aiming at the discovery and monitoring of Cepheids in NGC 300. As mentioned in the Introduction, these data have already been used by Pietrzyński et al. (2001) to identify OB associations in NGC 300. Improved *BVI* stellar photometry has been measured for the current work with DAOPHOT/ALLSTAR on a subset (about 20 nights) of the entire dataset, leading to a zero-point accuracy of ~ 0.03 mag. For further details on the stellar photometry the reader is referred to Pietrzyński et al. (2001).

For a preliminary catalog of blue supergiant candidates we selected all stars brighter than $V = 20$, corresponding to an absolute magnitude $M_V = -6.5$ (luminosity class Iab or brighter for B- and A-type stars) for an adopted distance modulus $m - M = 26.53$ (Freedman et al. 2001), and having color index in the range $-0.3 < B - V < 0.3$. At this high galactic latitude ($b = -79^\circ$) the foreground reddening is low, around $E(B - V) = 0.02$ (Burstein & Heiles 1984). This, combined with low internal reddening, makes the observed $B - V$ closely corresponding to the intrinsic stellar color, and our criterion is therefore optimal for isolating late B- and early A-type supergiants. The final list of candidates for the spectroscopic follow-up, containing 167 objects, was set up by carefully examining the original WFI frames, rejecting objects on the basis of broad profiles and presence of nearby companions. An $H\alpha$ image of the galaxy was also inspected in order to avoid overlap with emission line nebulae.

Spectroscopy of a subset of our candidate list was obtained with Antu and FORS1 at the Very Large Telescope (Paranal) on September 25 and 26, 2000. Two FORS1 fields were observed each night in multi-object spectroscopy mode, allowing simultaneous spectroscopy of 19 objects, for a total of four different pointings, chosen to allow a good coverage of the radial extent of the galaxy. Sky and seeing conditions were excellent on both nights, with typical 0.7 arcsec seeing, but with long spells of 0.4–0.5 arcsec seeing. Five exposures, each lasting 45 min, were secured at every pointing with a 600 gr/mm grating, which provides approximately a 5 Å spectral resolution. The spectral coverage with this setup is about

1,000 Å wide, centered around 4,500 Å (dependent on an object’s position in the focal field along the dispersion axis), including in most cases the range from the H and K calcium lines up to the Balmer H β line.

Due to the positioning limitations of the FORS slitlets and the uneven distribution of blue supergiants in NGC 300, a few additional objects, not included in our candidate list, were also observed. Among these were H II regions, blue stars somewhat fainter than our original magnitude limit, and a handful of late-type stars. Central coordinates of the fields observed are reported in Table 1, while Fig. 1 shows the location of these fields on a wide-field image of NGC 300. The individual fields, together with the identification of the spectroscopic targets, are shown in Fig. 2 through 5, reproducing *V*-band, 5-min FORS1 exposures. Table 2 summarizes the positions, *BVI* magnitudes and additional information for all the objects for which a spectrum was obtained. In this Table and for the rest of this paper, individual stars will be identified with the letter corresponding to the galaxy field (A through D) and the progressive FORS slitlet number (1 through 19).

The generic image processing tasks within IRAF⁴ were used for bias and flat field corrections. After adding all the images of a given field, each individual slitlet spectrum was treated as a long-slit spectrum, and independently wavelength calibrated and extracted. Finally, the 1-D spectra were normalized with a low-order polynomial. Our targets are mostly located in uncrowded regions, so that sky subtraction did not pose particular problems. The only difficult cases were represented by stars in the proximity of or within emission nebulae. Despite our efforts to avoid such occurrences by using the H α image of NGC 300, the spectra of several stars were found to be contaminated by nebular emission. At this spectral resolution a complete and satisfactory subtraction of this contamination is not possible, and we marked the affected objects in Table 2. The average S/N for most of the spectra is close to 50, but for the brightest stars it goes up to $\simeq 100$. Only very few spectra are underexposed (S/N < 25).

3. Spectral classification

The spectral classification of our targets was carried out by a visual comparison of the observed spectra with template spectra of B- and A-type Galactic supergiants, and B-type supergiants in the SMC, degraded to FORS resolution. While the SMC data have been taken from the literature (Lennon 1997), the Galactic data are part of an ongoing project, which

⁴IRAF is distributed by the National Optical Astronomy Observatories, which are operated by AURA, Inc., under contract with the National Science Foundation.

aims at obtaining high-resolution spectra of nearby blue supergiants for accurate stellar atmospheric analysis. The overall appearance of the available spectra compared with the template spectra was used for the spectral classification, with special attention to widely-used diagnostics of blue supergiants.

As pointed out by Lennon (1997), ambiguities in the spectral classification of extra-galactic B-supergiants can arise if the classification scheme does not account for possible significant deviations from galactic metallicity. We have therefore applied his classification criteria, which are more independent of metallicity, and have used both sets of templates, Galactic and SMC, for B-type spectra. However, in a few cases ambiguities remained, which we will be able to eliminate only after a detailed quantitative analysis of the spectra has been carried out. Those cases are marked in Table 2 and the comparison shows a relatively small effect (a shift of one or two subclasses) due to the different metallicity of the template spectra.

The spectral types thus determined are presented in column 7 of Table 2. In several cases we provide a range of spectral classes, reflecting the uncertainty due to the S/N of the spectra and the possible abundance effects. Additional comments pertaining to the appearance of the spectra or the spectral classification are given in column 8. Objects which show a possibly composite spectrum were not assigned a spectral classification. The nebular contamination has been identified as such when the 2-D spectra indicated the presence of emission lines extending over and beyond the stellar position.

We present in Figs. 6-12 the spectra of the NGC 300 supergiants, grouped by spectral type as follows: late-O and early-B (B0 through B5), late-B, early-A (A0 through A5), late-A and F stars. We exclude from this spectral atlas the H II region spectra, and some additional objects, which include a foreground white dwarf and a WN11 star, which will be discussed in a future paper.

The position of the supergiant sample in the HRD is shown in Fig. 13. The stellar luminosity was derived after correcting for reddening (assuming $A_V = 3.1 E(B - V)$). The latter was obtained from the observed $B - V$ and the expected value of this color index for a given spectral type, as given by Fitzgerald (1970). Bolometric corrections and effective temperatures as a function of spectral type were taken from Humphreys & McElroy (1984). Theoretical stellar tracks at metallicity $Z=0.008$ from Schaerer et al. (1993) are also shown for comparison (the new tracks which include stellar rotation by the Geneva group and used in Sect. 4.1 to estimate the stellar parameters of two bright supergiants are not yet available for this metallicity). The apparent gap centered around $\log T_{eff}=4.1$ is the result of a selection effect, due to the lack of template spectra between types B5 and B8 in our classification program.

4. First results

4.1. Stellar parameters and abundances

While at the resolution currently attainable in multiobject spectroscopy of targets as faint as our blue supergiants a detailed chemical abundance analysis is difficult (though not impossible), we can in any case estimate, within roughly 0.2 dex, the abundances of several elements by a comparison of the observed spectra to synthetic ones generated by models of blue supergiant atmospheres, calculated for a variety of metal abundances. We leave a full abundance analysis of our blue supergiant sample to a forthcoming paper, but we want to show here some first results illustrating the power of our technique to estimate the metal abundances of these stars.

The photospheric analyses are performed on the basis of hydrostatic LTE line-blanketed model atmospheres (Kurucz 1991) and subsequent non-LTE/LTE spectrum synthesis. Effective temperatures T_{eff} are estimated from the spectral classification, and surface gravities $\log g$ are determined from the Balmer line strengths; the microturbulence ξ is assumed to be the same as in the Galactic comparisons. The helium content y (by number) and the stellar metallicity $[M/H]$ are deduced from the comparison of the observed and the synthetic spectra for varying elemental abundances. At present, the elements with strong lines in A-type stars, e.g. Mg II, Ti II and Fe II, are treated in non-LTE, while Si II and Cr II are treated in LTE. In total, several ten-thousand lines from these and some 20 other chemical species – comprising almost all spectral features – are included in the spectrum synthesis (with the CNO and S lines also in non-LTE). The results from the analysis of two of the NGC 300 supergiants, A-8 and D-13, are summarized in Table 3. Radial velocities v_{rad} can be determined from cross-correlation of the observed spectra with the synthetic ones.

In Fig. 14 we show the observed spectrum of the A0 Ia star A-8, together with model fits which were calculated for three different metal abundances: 0.2, 0.5 and 1.0 solar. A comparison of the predicted and observed line intensities, particularly for lines of elements Fe and Cr, suggests a low abundance for this star, in the order of 0.2 solar. This is consistent with the star’s position in the outskirts of the galaxy, where a low metal abundance would be expected. In Fig. 15 we show the same model fits to the spectrum of another A0 supergiant, star D-13. This object has a clearly higher metal abundance, in the order of 0.5 solar. Again this is consistent with the expected higher metallicity for this star, which is considerably closer to the center of NGC 300. In both figures the estimated noise level in the continuum (1%) is shown by vertical bars at the lower left. An additional 1% uncertainty is estimated for the placement of the continuum. The latter was measured from low-order polynomial fits to relatively line-free regions of the observed spectra, where the theoretical normalized

fluxes predicted for different metallicities reach unity simultaneously (e.g. around 4160 Å, 4200 Å, 4610 Å, 4690 Å). This is contrast with the situation in the UV part of the spectrum, where the ‘true’ continuum is never observed (Haser et al. 1998).

Applying the technique described above to the complete sample of supergiants, we expect to delineate the radial metallicity gradient in the disk of NGC 300 rather accurately. It will be of considerable interest to compare the stellar abundance gradient to the one derived from H II region abundance studies, which in extragalactic work has been assumed to reflect the stellar abundances, e.g. in the work of the HST Key Project team on M101 to measure the metallicity effect on the Cepheid PL relation (Kennicutt et al. 1998).

Having determined the atmospheric parameters, the physical properties of the stars are derived, cf. Table 3. The reddening $E(B - V)$ is found from the comparison of the photometry with the synthetic colors from the model fluxes. Absolute visual magnitudes M_V are obtained after correcting for extinction, assuming $A_V = 3.1 E(B - V)$. Applying a bolometric correction $B.C.$ leads to the stellar bolometric magnitude M_{bol} . From this and the atmospheric parameters T_{eff} and g , the stellar luminosity L , the radius R and the spectroscopic mass M^{spec} are determined. Zero-age main sequence masses M^{ZAMS} are derived from comparison with stellar evolution tracks accounting for mass-loss and rotation (Meynet & Maeder 2000; Maeder & Meynet 2001). The supergiant A-8 is situated in a region of the HRD where partial blue loops may be found in stellar evolution calculations, depending on the detailed physics accounted for (see discussion in Maeder & Meynet 2001). An enhanced He abundance supports such an interpretation for the evolutionary status of this object (cf. the 12 M_\odot track of Maeder & Meynet 2001). The more massive supergiant D-13 has either developed directly from the main sequence (in the case of an initially fast rotator) or has reached the post red supergiant phase (as an initially slow rotator), accounting for its marked helium enhancement and its spectroscopic mass (cf. the 20 M_\odot track of Meynet & Maeder 2000). Note that for this metallicity sophisticated stellar evolution tracks accounting for rotation are not available yet, but those for solar metallicity are expected to be sufficiently similar. Unfortunately, information on the N/C ratio, the most sensitive indicator on the evolutionary status, cannot be derived from the available spectra.

To conclude, the wealth of data obtained on just two sample supergiants clearly demonstrates the versatility of quantitative spectroscopy for stellar and – through the observation of a larger ensemble of objects – galactic studies.

4.2. Wind Momentum-Luminosity Relationship (WLR)

The existence of a relationship between the stellar wind momentum and the luminosity of hot massive stars is a sound prediction of the theory of radiatively driven winds (Kudritzki 1998, Kudritzki & Puls 2000). The relationship has the form

$$\dot{M}v_{\infty} \propto R^{-0.5} L^{1/\alpha}$$

where the product of mass-loss rate (\dot{M}) and the wind terminal velocity (v_{∞}) gives the mechanical momentum flow carried away by the stellar wind. R is the stellar radius, L the luminosity, and α is the exponent of the power-law line strength distribution function of the metal lines driving the wind. As the ionizing properties in the stellar atmosphere change with effective temperature, so do the line strengths of the metal lines most effective at driving the wind, and as a consequence α is expected to vary with stellar spectral type, and values from ~ 0.65 (O-type) to ~ 0.38 (A-type) are found in the solar neighborhood (Kudritzki & Puls 2000).

The validity of the WLR has been demonstrated empirically by Puls et al. (1996) for O-type stars in the Galaxy and the Magellanic Clouds, as well as for Galactic supergiants of type B and A (Kudritzki et al. 1999), confirming the expected dependence of the relation on spectral type, roughly in agreement with the slopes predicted by theory. Our new, large sample of blue supergiants in NGC 300, all at a given distance (which will eventually be improved with the Cepheids we are currently detecting in a parallel program) provides an extremely valuable dataset to improve the calibration of the WLR and establish its dependence on spectral type and metallicity, with a much higher accuracy than hitherto possible. The most accurate results for the wind momentum of the blue supergiants can be obtained from a modeling of the Balmer $H\alpha$ line profile (for a review, see Kudritzki & Puls 2000), and we are looking forward to getting red spectra covering $H\alpha$ for our complete sample of blue supergiants with VLT later this year. However, for the brightest stars it is possible to derive the wind momentum also from the $H\beta$ line, albeit with lower accuracy. We have done this for the A2 supergiant D-12. This star has an absolute visual magnitude $M_V = -8.35$, and is one of the brightest supergiants in our sample. From a fit to the $H\beta$ line profile, the mass-loss rate was obtained $(1.8 (\pm 0.2) \times 10^{-6} \text{ M}_{\odot}/\text{yr})$, which, together with an assumed value for v_{∞} (150 km/s, a typical value for A2 supergiants, cf. Lamers et al. 1995 and Kudritzki & Puls 2000) and radius ($210 R_{\odot}$, derived from $E(B-V) = 0.15$, $M_V = -8.35$ and model atmosphere flux), yielded the position in the diagnostic diagram shown in Fig. 16. It is seen that this ‘preliminary’ datapoint from this one supergiant fits relatively well into the existing WLR for A supergiants, making us optimistic that we can achieve a significant

improvement on the WLR with the results based on the $H\alpha$ profiles.

5. Conclusions

We have presented a spectral catalog of about 70 blue supergiant candidates in NGC 300, observed at a resolution $R \simeq 1000$ and S/N $\simeq 50$ in the 4,000-5,000 Å spectral range at the VLT. Of the observed targets, 62 are spectroscopically confirmed as supergiants with spectral types between late-O and F. Most of these supergiants are types B and A. In our survey, we also found several different, interesting objects including a WN11 star and a foreground white dwarf, which will be analyzed in detail in forthcoming studies. The spectral classification of the blue supergiants determined in this paper will be essential for a thorough investigation of the dependence of the wind momentum-luminosity relationship as a new, purely spectroscopic and far-reaching distance indicator on spectral type, as predicted by theory, and seen in preliminary empirical results (Kudritzki et al. 1999).

A model atmosphere technique was employed to obtain first results for the metal abundances of two A0 supergiants in our sample. A comparison of synthetic spectra, calculated for different metal abundances, with the observed spectra of these stars, yields metal abundances different by approx 0.3 dex in the expected sense that the star closer to the center of NGC 300 is more metal-rich than its counterpart, which is located at a larger galactocentric distance. In a forthcoming paper we will use this technique on the whole sample of blue supergiants in NGC 300 to determine their metal abundances. While the individual values of these abundances will be of a modest accuracy (about ± 0.2 dex per star), the large number of stars in our sample and the wide range in galactocentric distance they span, should allow us to determine the abundance gradient in the disk of NGC 300 with an accuracy which is unprecedented in the study of spiral galaxies beyond the Local Group.

We also report on a first determination of the wind momentum for one of the brightest A-type supergiants in our sample, based on its mass-loss rate as determined from the Balmer $H\beta$ line profile, and find that it fits relatively well into the empirical WLR determined from A supergiants in the Galaxy and M31 by Kudritzki et al. (1999). We will be able to obtain the wind parameters with higher accuracy from $H\alpha$ profiles which we expect to have at our disposal, for all stars in our sample, by the end of 2001. We will then be able to perform a thorough empirical check of the usefulness of the WLR for distance determinations, including a calibration of its dependence on spectral type and metallicity, and of its intrinsic dispersion, for a given spectral type and metallicity.

FB acknowledges DLR grant 50 OR 9909 for support while working in Munich. WG

gratefully acknowledges financial support received from Fondecyt grants 1000330 and 8000002 for this project. Part of this work was done while he was a scientific visitor at ESO Garching. WG is grateful for the support received from ESO. We also thank the referee, A. de Koter, for positive and constructing comments.

REFERENCES

- Bresolin, F., Kudritzki, R.P., Mendez, R.H., & Przybilla, N., 2001, *ApJ*, 548, L159
- Burstein, D. & Heiles, C., 1984, *ApJS*, 54, 33
- Dufton, P. L., McErlean, N. D., Lennon, D. J., & Ryans, R. S. I., 2000, *A&A*, 353, 311
- FitzGerald, M.P., 1970, *A&A*, 4, 234
- Freedman, W. L., Madore, B. F., Gibson, B. K., et al., 2001, *ApJ*, 553, 47
- Haser, S.M., Pauldrach, A., Lennon, D.J., Kudritzki, R.P., Lennon, M., Puls, J., & Voels, S.A., 1998, *A&A*, 330, 285
- Humphreys, R.M. & McElroy, D.B., 1984, *ApJ*, 284, 565
- Kennicutt, R.C., Stetson, P.B., Saha, A., et al., 1998, *ApJ*, 498, 181
- de Koter, A., Heap, S. & Hubeny, I., 1998, *ApJ*, 509, 879
- Kudritzki, R. P., Cabanne, M.L., Husfeld, D., Niemela, V.S., Groth, H.G., Puls, J., Herrero, A. , 1989, *A&A*, 226, 235
- Kudritzki, R. P., 1998, in *Stellar Astrophysics for the Local Group* (eds Aparicio, A., Herrero, A. & Sanchez, F.) 149-262 (Cambridge University Press, Cambridge)
- Kudritzki, R. P., Puls, J., Lennon, D. J., Venn, K. A., Reetz, J., Najarro, F., McCarthy, J. K., & Herrero, A., 1999, *A&A*, 350, 970
- Kudritzki, R. P. & Puls, J., 2000, *ARA&A*, 38, 613
- Kurucz, R. L., 1991, in *Stellar Atmospheres: Beyond Classical Models* (eds L. Crivellari, I. Hubeny, & D.G. Hummer) (NATO ASI Ser. C, 341; Dordrecht: Kluwer), p. 441-447
- Lamers, H.J.G.L.M., Snow, T.P., & Lindholm, D.M. 1995, *ApJ*, 455, 269

- Lennon, D.J., Becker, S.T., Butler, K., Eber, F., Groth, H.G., Kunze, D., Kudritzki, R.P., 1991, *A&A*, 252, 498
- Lennon, D.J., 1997, *A&A*, 317, 871
- Maeder, A., & Meynet, G., 2001, *A&A*, 373, 555
- Meynet, G., & Maeder, A., 2000, *A&A*, 361, 101
- McCarthy, J. K., Lennon, D. J., Venn, K. A., Kudritzki, R. P., Puls, J., & Najarro, F., 1995, *ApJ*, 455, 135
- McCarthy, J. K., Kudritzki, R. P., Lennon, D. J., Venn, K. A. & Puls, J., 1997, *ApJ*, 482, 757
- Monteverde, M. I., Herrero, A., Lennon D. J., & Kudritzki, R. P., 1997, *ApJ*, 474, 107
- Monteverde, M. I., Herrero, A. & Lennon D. J., 2000, *ApJ*, 545, 813
- Muschiello, B., Kudritzki, R. P., Appenzeller, I., et al., 1999, *A&A*, 352, 40
- Pietrzyński, G., Gieren, W., Fouqué, P., & Pont, F., 2001, *A&A*, 371, 497
- Puls, J., Kudritzki, R. P., Herrero, A., et al., 1996, *A&A*, 305, 171
- Rolleston, W. R. J., Dufton, P. ., McErlean, N. D., et al., 1999, *A&A*, 348, 728
- Schaerer, D., Meynet, G., Maeder, A. & Schaller, G. 1993, *A&AS*, 98, 523
- Schmidt-Kaler, Th., 1982, in *Landolt-Börnstein, Neue Serie, Gruppe VI, Vol. 2b* (Berlin: Springer), p. 451
- Smartt, S. J., Crowther, P. A., Dufton, P. L., Lennon, D. J., Kudritzki, R. P., Herrero, A., McCarthy, J. K., & Bresolin, F., 2000, *MNRAS*, 325, 257
- Venn, K. A., 1999, *ApJ*, 518, 405
- Venn, K. A., McCarthy, J. K., Lennon, D. J., Przybilla, N., Kudritzki, R. P., & Lemke, M., 2000, *ApJ*, 541, 610
- Venn, K. A., Lennon, D.J., Kaufer, A., McCarthy, J. K., Przybilla, N., Kudritzki, R. P., Lemke, M., Skillman, E.D. & Smartt, S.J., 2001, *ApJ*, 547, 765

Fig. 1.— The four FORS1 fields observed in NGC 300 are marked on a montage of eight B-band ESO/MPI 2.2m + WFI frames. North is at the top, east to the left. Field size is approximately $34' \times 33'$.

Fig. 2.— Field A from a 5-min, V-band FORS1 exposure. The field of view is approximately $6.8' \times 6.8'$. The multi-object spectroscopy targets are marked by the circles. Their identification numbers correspond to those in Table 2.

Fig. 3.— Field B. The multi-object spectroscopy targets are marked by the circles. A bright foreground star has been masked out using one arm of the FORS MOS unit.

Fig. 4.— Field C. The multi-object spectroscopy targets are marked by the circles.

Fig. 5.— Field D. The multi-object spectroscopy targets are marked by the circles. A bright foreground star has been masked out using two arms of the FORS MOS unit.

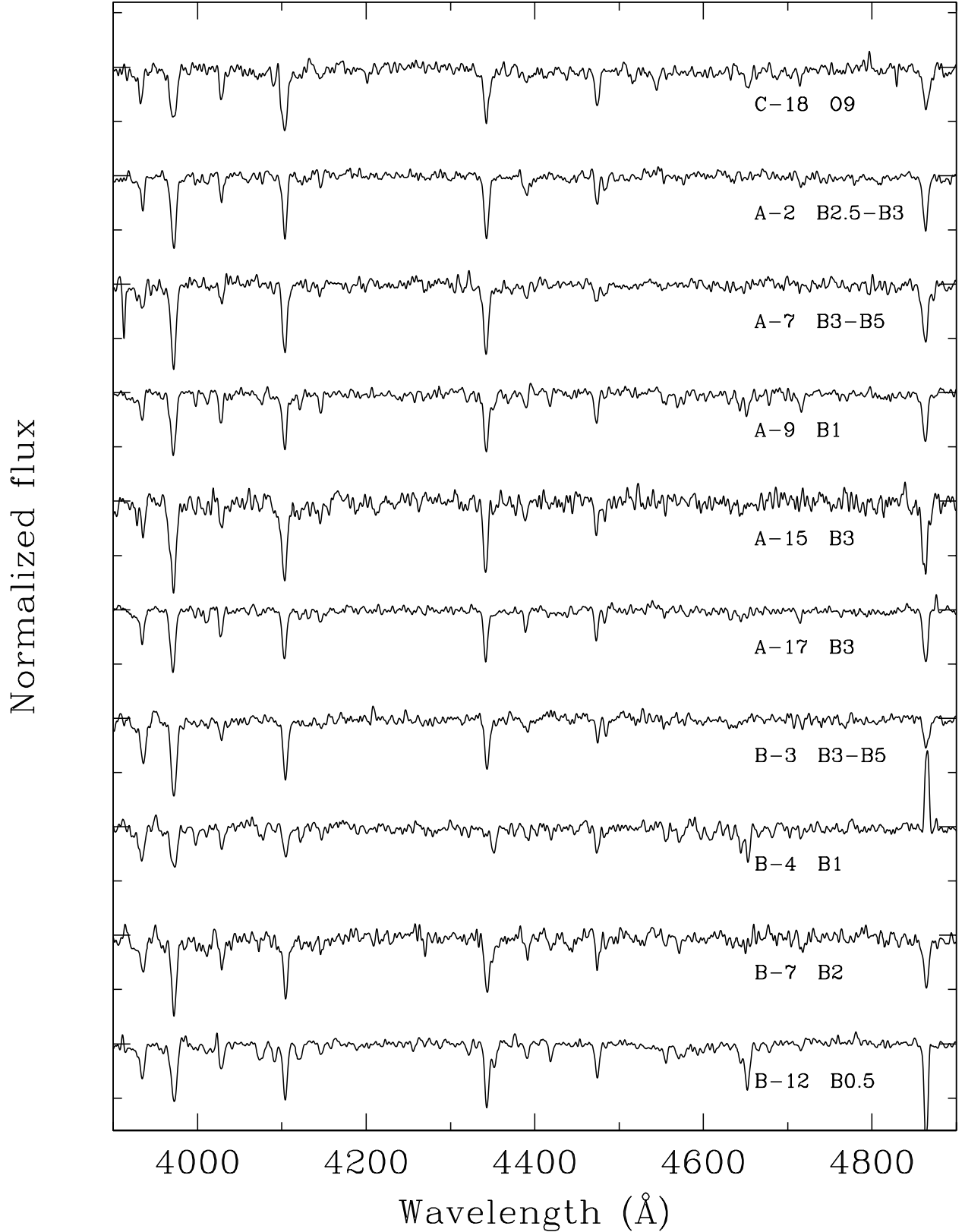


Fig. 6.— Spectral catalog of early-B supergiant stars in NGC 300. The first object is an O9 star. In this and all following figures the spectra are not displayed in the NGC 300 rest frame.

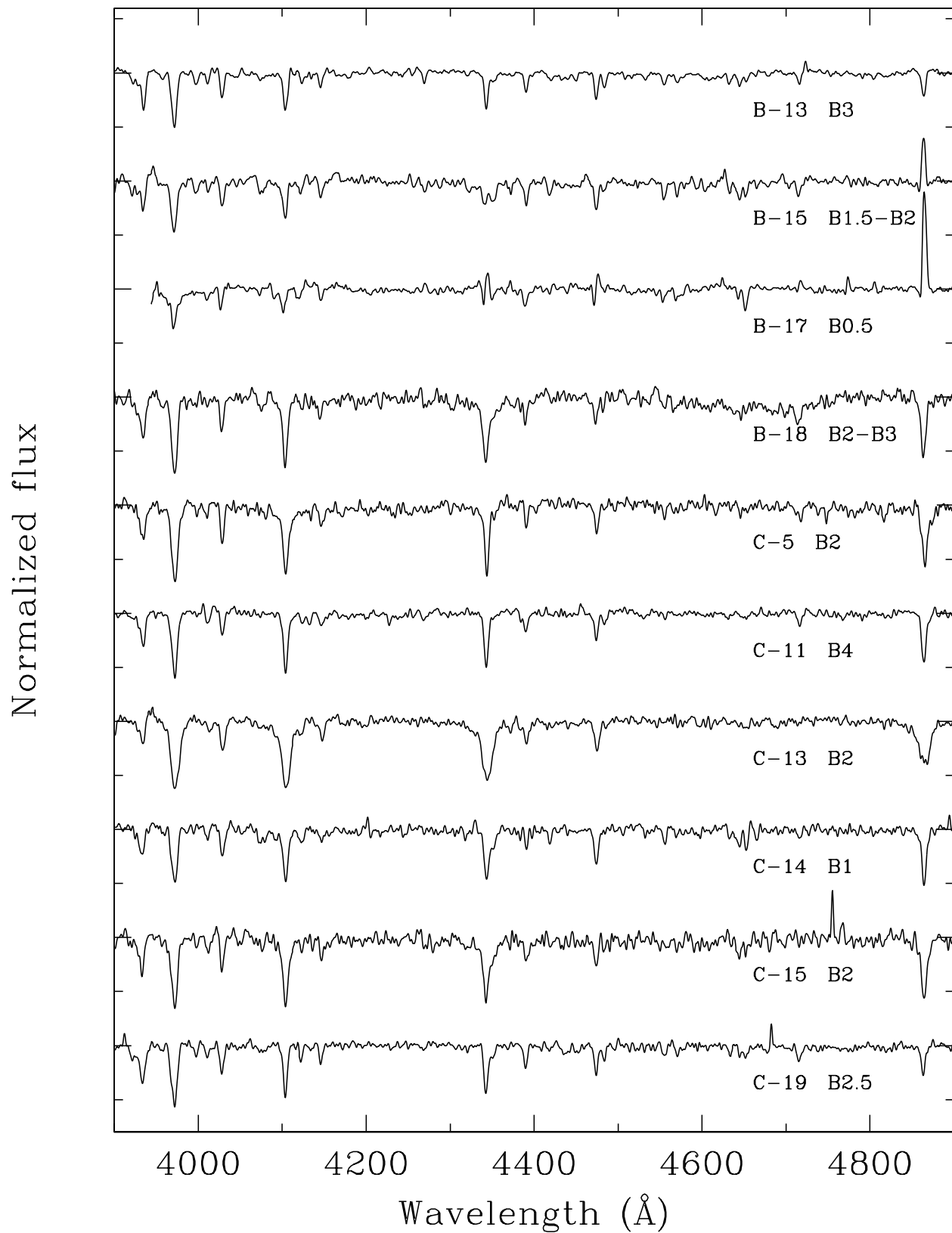


Fig. 7.— Spectral catalog of early-B supergiant stars in NGC 300.

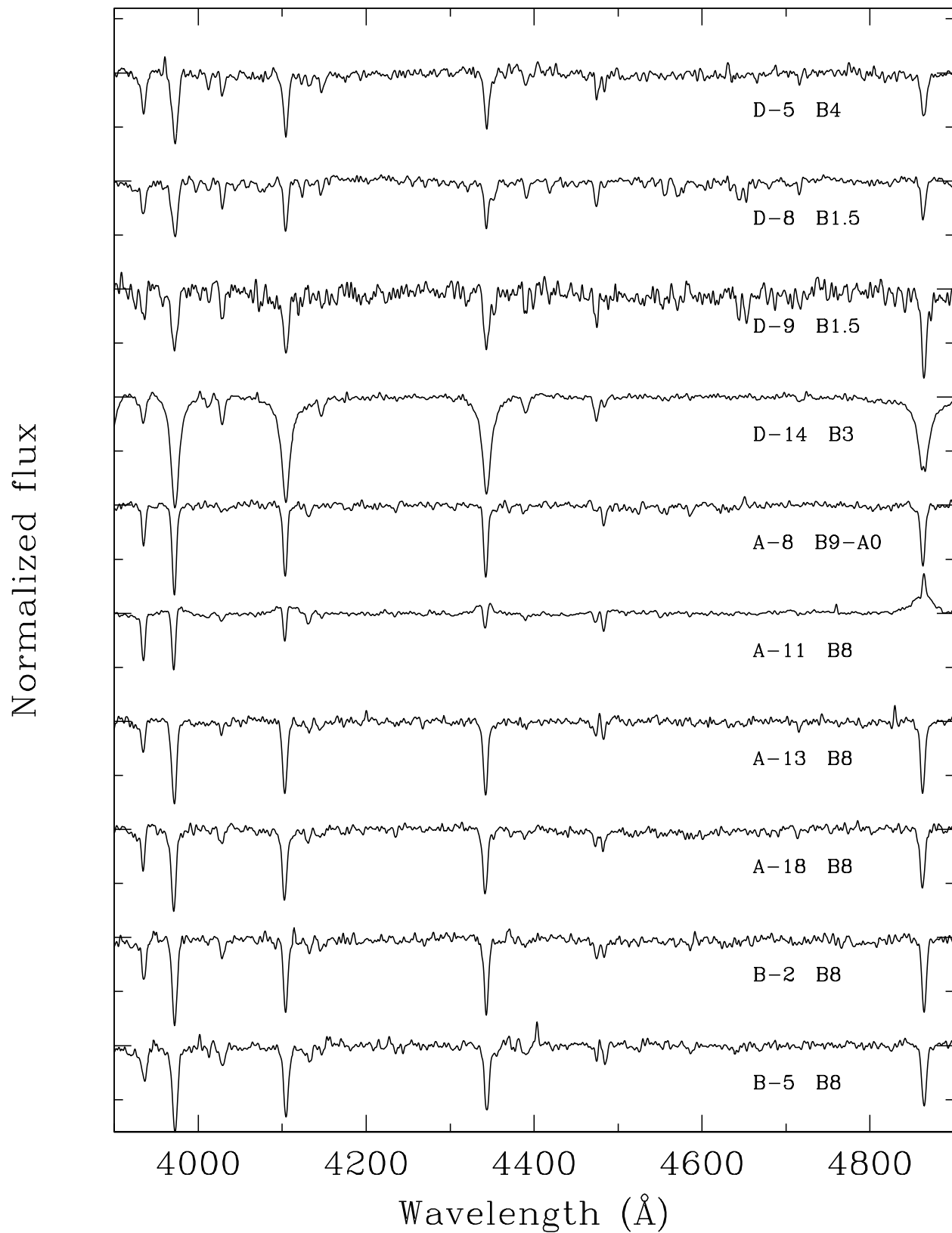


Fig. 8.— Spectral catalog of early- and late-B supergiant stars in NGC 300.

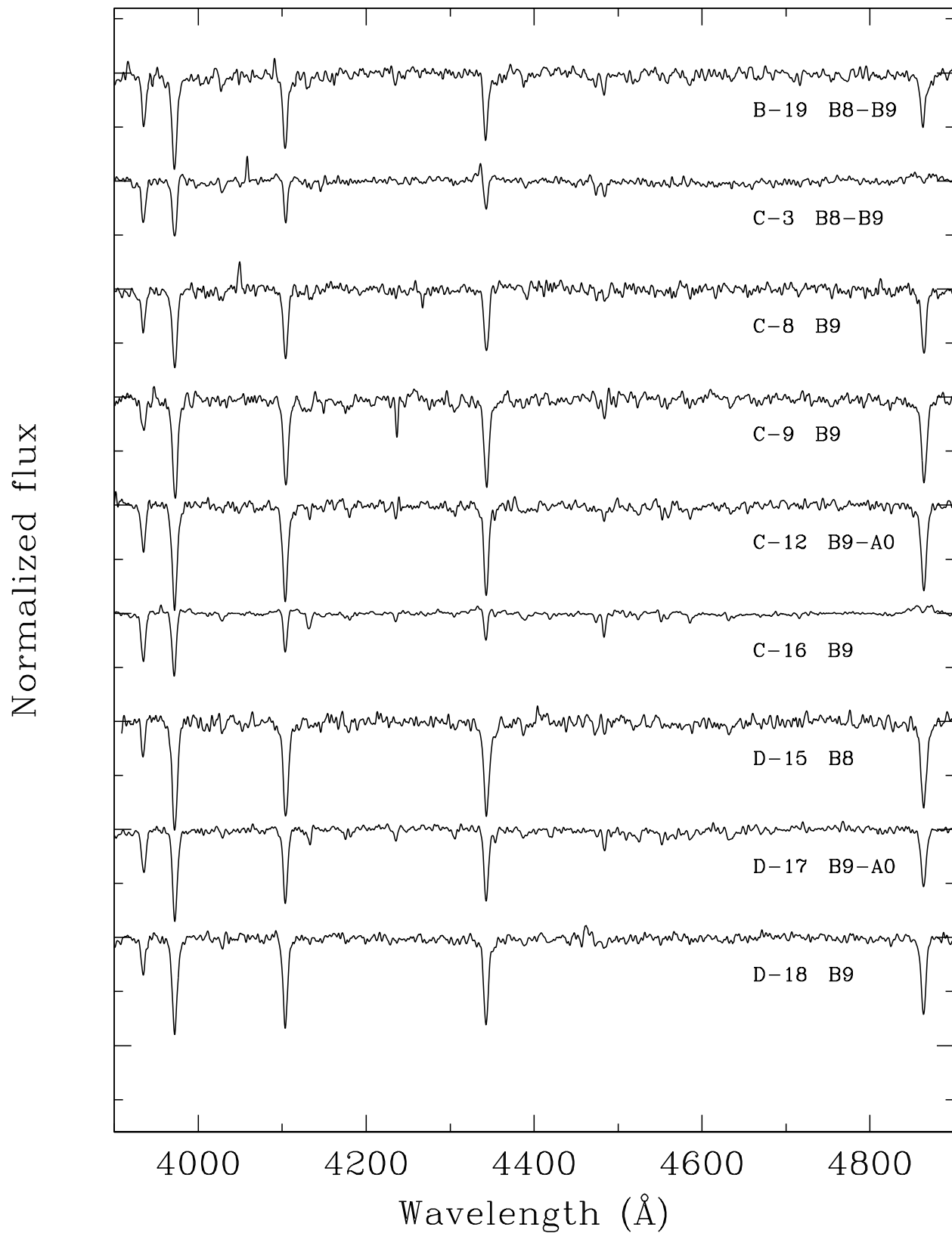


Fig. 9.— Spectral catalog of late-B supergiant stars in NGC 300.

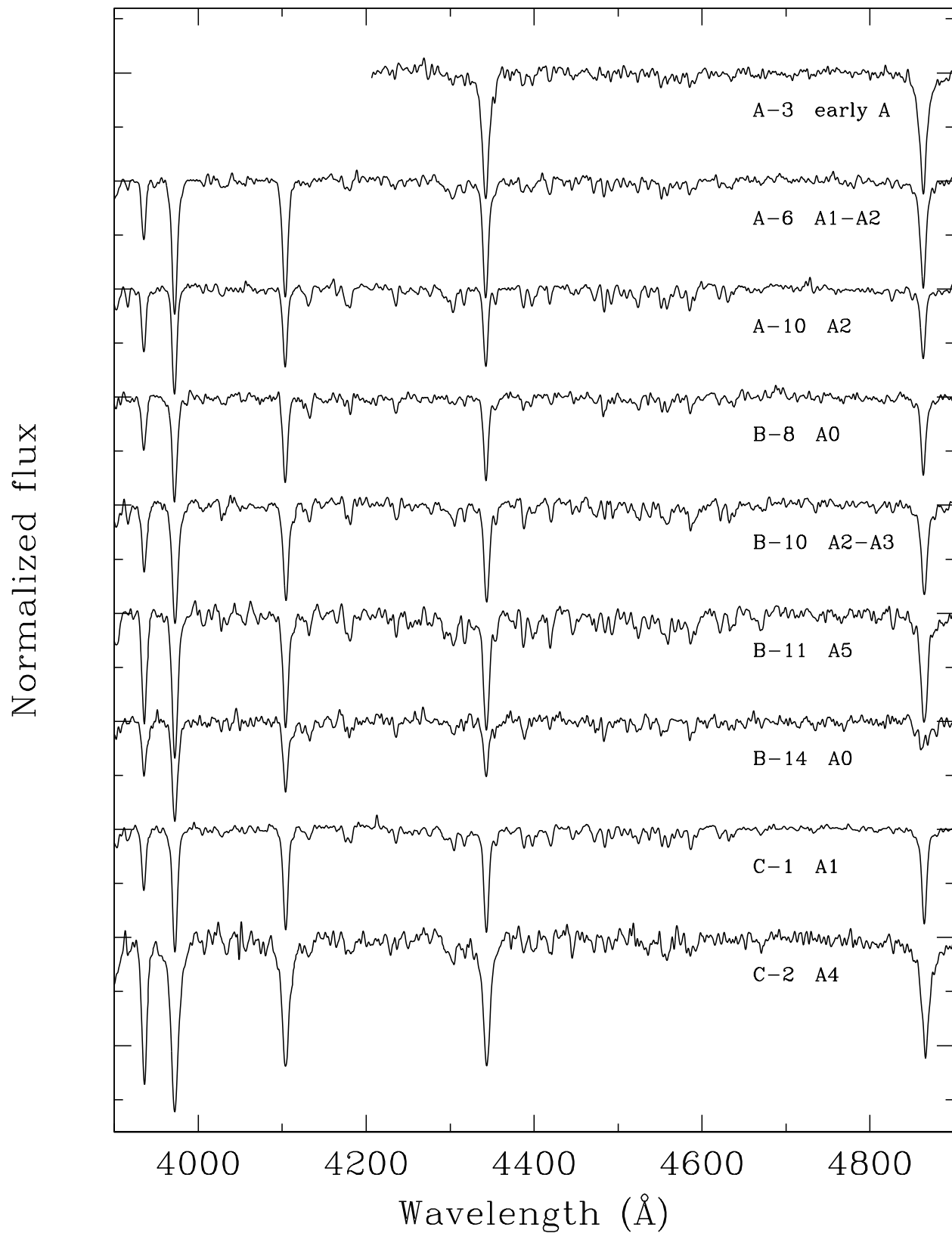


Fig. 10.— Spectral catalog of early-A supergiant stars in NGC 300.

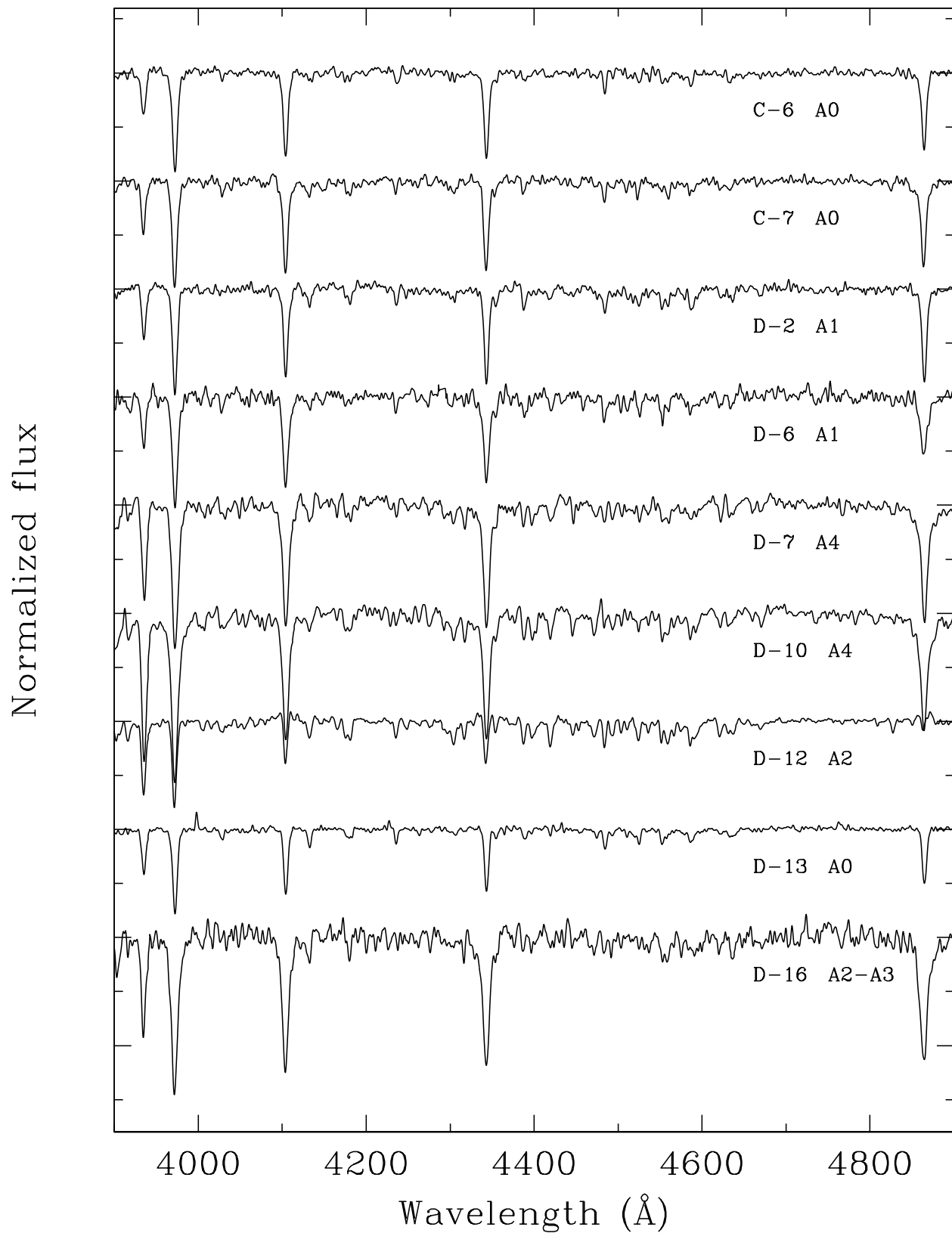


Fig. 11.— Spectral catalog of early-A supergiant stars in NGC 300.

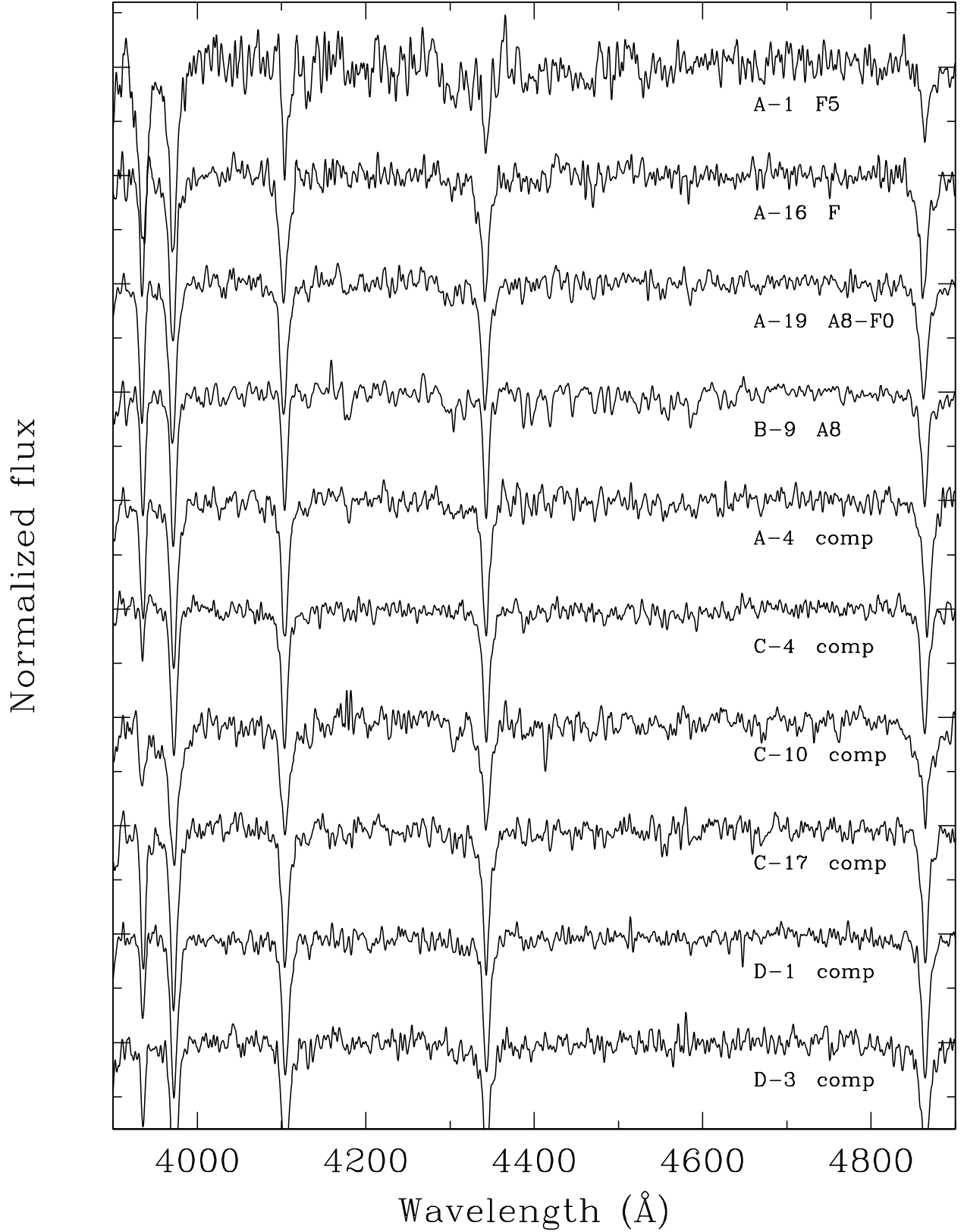


Fig. 12.— Spectral catalog of late-A and F supergiant stars in NGC 300, and several possibly composite spectra.

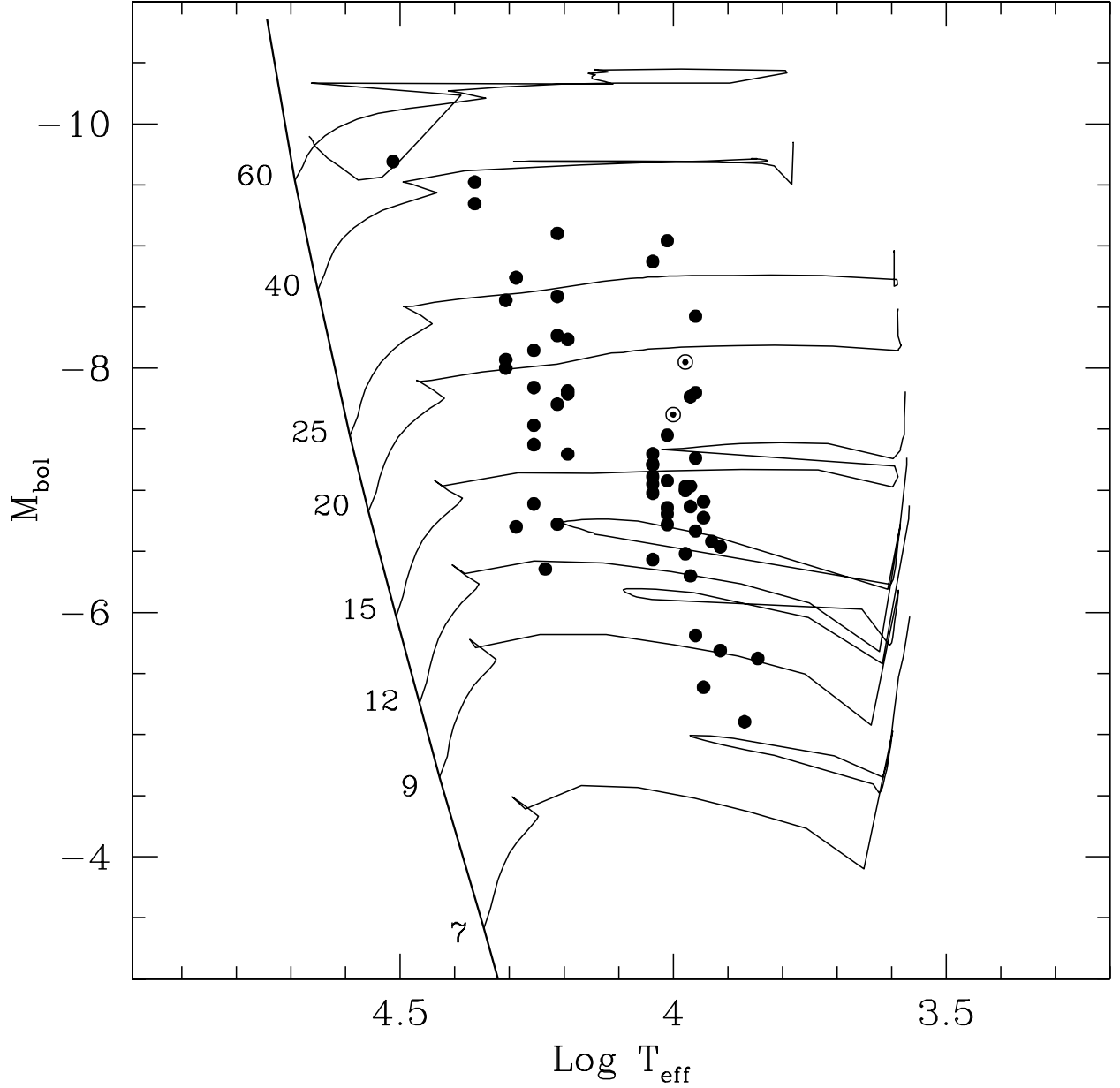


Fig. 13.— M_{bol} vs. T_{eff} diagram of the blue supergiants observed in NGC 300. The model tracks at metallicity $Z=0.008$ of Schaerer et al. (1993) for different initial stellar masses are shown, as indicated by the numbers to the left of the Main Sequence. The gap around $\log T_{eff}=4.1$ is due to the unavailability of spectral templates between types B5 and B8 in our spectral classification program. The two stars described in Sec. 4.1 are shown with different symbols.

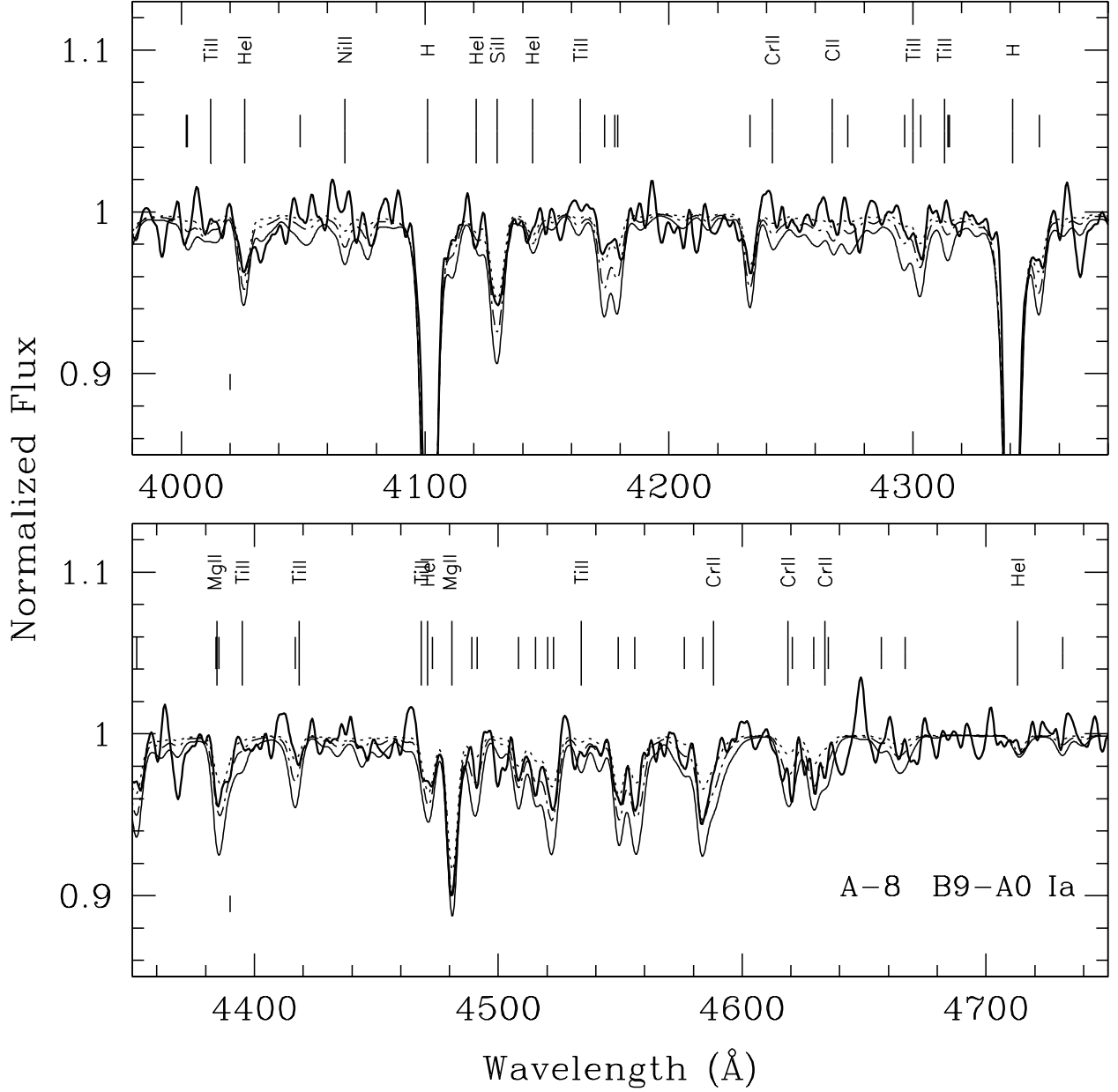


Fig. 14.— Model fits, corresponding to metal abundances of 0.2, 0.5 and 1.0 solar (dotted, dashed and solid lines, respectively), to the spectrum of the B9-A0 supergiant A-8 in NGC 300 (thick solid line). Short vertical marks in the element identification section indicate Fe II lines. The metal abundance of this star is ~ 0.2 solar. The estimated 1% noise level in the continuum is shown by the bar at the lower left of each plot.

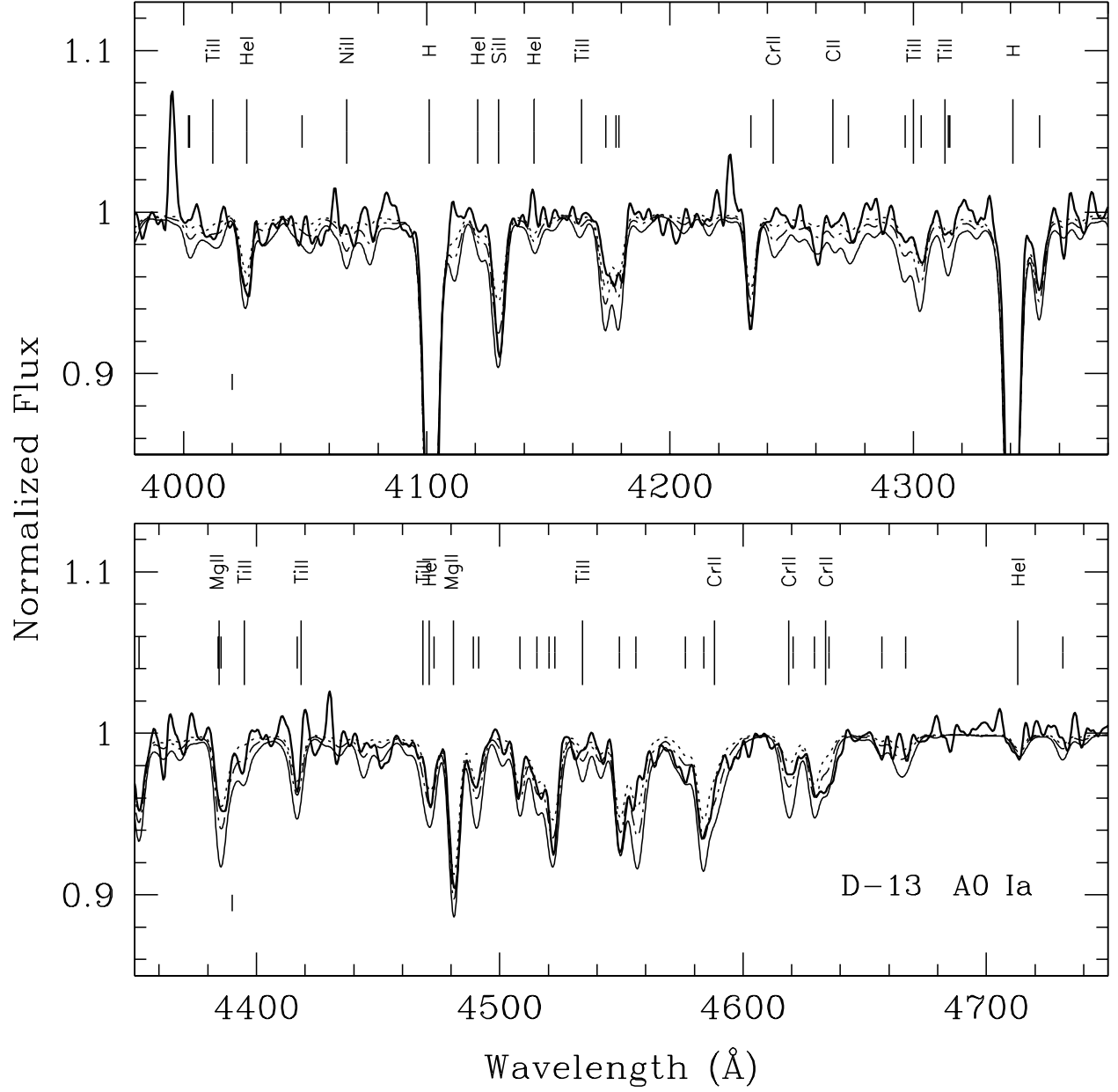


Fig. 15.— As Fig. 13, for the A0 supergiant D-13. The metal abundance of this star is higher than that of A-8, ~ 0.5 solar.

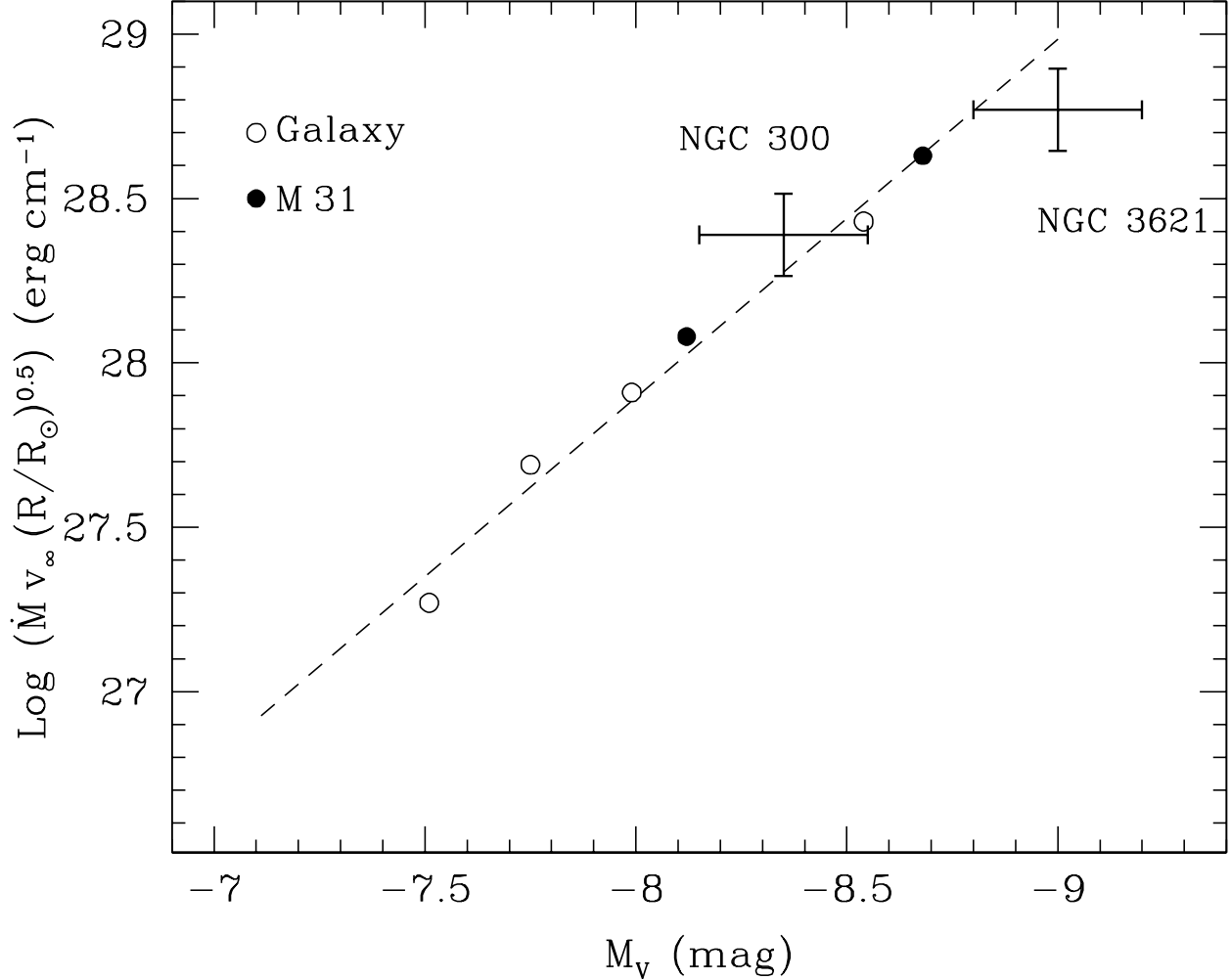


Fig. 16.— Wind momentum-luminosity relationship for A-type supergiants taken from data of Galactic (open circles) and M31 (filled circles) supergiants (data taken from Kudritzki et al. 1999; improved photometry and distance modulus were used for M31, see Bresolin et al. 2001). Also plotted is the A0 supergiant examined by Bresolin et al. (2001) in NGC 3621, and star D-12 in NGC 300 analyzed in this paper.

Table 1. NGC 300 - Observed fields

Field	RA (2000.0)	DEC (2000.0)	Position Angle (deg)	Obs. date
A	00 55 36.4	−37 41 36.5	0	Sep. 25, 2000
B	00 54 52.1	−37 40 26.9	0	Sep. 25, 2000
C	00 54 32.4	−37 36 16.7	20	Sep. 26, 2000
D	00 54 30.6	−37 42 21.7	−13	Sep. 26, 2000

Table 2. NGC 300 - Spectroscopic targets

Slit no.	RA	DEC	V	$B - V$	$V - I$	Spec. type	Comments
FIELD A							
1	0 55 37.069	−37 38 19.44	21.50	0.49	0.60	F5	noisy
2	0 55 36.674	−37 38 31.03	20.04	−0.11	−0.05	B2.5–B3	Balmer lines stronger than standards
3	0 55 47.220	−37 38 50.51	20.10	0.07	0.21	early A	spectrum incomplete, Balmer lines strong, composite?
4	0 55 22.188	−37 39 17.08	20.86	0.12	0.31		noisy, Balmer lines strong, composite?
5	0 55 32.104	−37 39 39.30	20.71	2.18	...		very noisy
6	0 55 37.828	−37 40 07.01	19.74	0.03	0.12	A1–A2	Si II 4128/32 missing, Mg II 4481 weak, metal weak? Balmer lines strong for Gal. abundance; B5–B8 if metal-poor
7	0 55 37.865	−37 40 23.20	20.43	−0.11	0.10	B3–B5	
8	0 55 41.619	−37 40 58.61	19.44	−0.01	...	B9–A0	
9	0 55 39.262	−37 41 18.23	20.23	−0.17	...	B1	
10	0 55 31.961	−37 41 38.33	18.98	0.07	...	A2	
11	0 55 38.317	−37 41 56.81	18.41	0.07	...	B8	emission wings in Balmer lines, H β in emission, very strong wind?
12	0 55 32.497	−37 42 26.62	19.49	0.14	−0.06		foreground white dwarf
13	0 55 33.276	−37 42 46.78	19.83	−0.06	−0.02	B8	Si II a little weak
14	0 55 33.921	−37 43 11.63	19.72	−0.26	...		H II region
15	0 55 31.716	−37 43 23.95	21.00	−0.12	...	B3	noisy, Balmer lines strong
16	0 55 29.379	−37 43 57.70	21.29	0.15	0.39	F Ib ?	Balmer lines strong
17	0 55 28.182	−37 44 23.41	19.78	−0.01	0.10	B3	
18	0 55 34.875	−37 44 48.15	19.99	−0.03	0.01	B8	
19	0 55 38.936	−37 44 57.33	20.75	0.12	...	A8–F0	
FIELD B							
1	0 55 00.217	−37 37 03.26	20.54	0.52	...	late-type	
2	0 55 01.823	−37 37 24.07	20.06	−0.08	0.05	B8	He I 4713 weak
3	0 54 46.351	−37 37 51.35	20.03	−0.08	0.06	B3–B5	He I 4121,4143 missing
4	0 54 51.799	−37 38 13.93	20.09	−0.05	...	B1	nebular contamination
5	0 54 44.166	−37 38 31.53	19.83	−0.04	−0.03	B8	
6	0 54 45.185	−37 38 47.96	18.97	−0.14	...		H II region
7	0 54 51.950	−37 39 23.85	20.45	−0.04	...	B2	somewhat noisy
8	0 55 00.527	−37 39 40.54	19.83	−0.01	...	A0	nebular contamination?
9	0 55 03.270	−37 39 56.00	19.97	0.16	0.33	A8	Balmer lines somewhat strong
10	0 54 47.072	−37 40 25.63	19.45	0.05	...	A2–A3	
11	0 54 47.310	−37 40 42.28	19.95	0.00	...	A5	
12	0 54 56.083	−37 41 04.02	19.30	−0.18	0.00	B0.5	
13	0 54 56.754	−37 41 33.79	18.64	−0.11	...	B3	Balmer lines filled
14	0 55 01.465	−37 41 46.80	19.86	0.04	...	A0	nebular contamination
15	0 55 03.464	−37 42 26.18	19.71	−0.06	...	B1.5–B2	nebular contamination
16	0 54 44.645	−37 42 39.13	19.02	−0.11	...		emission line object, WN11
17	0 55 04.077	−37 42 53.99	19.37	−0.10	...	B0.5	Balmer lines filled, P Cyg profiles at He I 4471,4713?
18	0 54 58.692	−37 43 21.06	20.35	−0.17	...	B2–B3	
19	0 54 57.705	−37 43 38.65	19.93	−0.05	...	B8–B9	
FIELD C							
1	0 54 27.873	−37 32 30.71	19.14	0.07	0.17	A1	Balmer lines strong
2	0 54 41.680	−37 33 45.40	21.28	0.09	0.38	A4	Balmer lines strong
3	0 54 36.242	−37 33 51.58	19.88	0.03	0.14	B8–B9	Si II weak, nebular contamination
4	0 54 41.759	−37 34 36.85	21.31	−0.03	0.13		composite?

Table 2—Continued

Slit no.	RA	DEC	V	$B - V$	$V - I$	Spec. type	Comments
5	0 54 31.834	−37 34 32.86	20.66	−0.12	0.40	B2	metal poor
6	0 54 33.190	−37 34 55.72	19.91	0.05	0.27	A0	metal depleted?
7	0 54 39.558	−37 35 39.28	20.35	0.00	0.15	A0	Balmer lines strong
8	0 54 23.455	−37 35 07.01	20.05	−0.05	0.08	B9	metal poor? Balmer lines strong
9	0 54 21.294	−37 35 17.93	20.25	0.02	0.19	B9	Balmer lines strong
10	0 54 32.431	−37 36 20.43	21.03	0.27	0.52		composite?
11	0 54 21.331	−37 35 56.24	19.66	−0.01	0.35	B4	
12	0 54 18.050	−37 36 09.71	20.16	0.02	0.19	B9–A0	Mg II weak
13	0 54 31.605	−37 37 44.29	19.75	−0.16	...	B2	Balmer lines broad, metal poor
14	0 54 26.881	−37 37 34.41	20.26	−0.18	−0.07	B1	
15	0 54 22.197	−37 37 44.98	20.99	−0.21	...	B2	for Gal. abundance, B1–B1.5 if metal-poor
16	0 54 21.938	−37 38 12.77	18.04	0.05	0.19	B9	Balmer lines filled
17	0 54 22.528	−37 38 25.50	20.97	0.13	0.31		composite?
18	0 54 25.855	−37 39 19.06	20.03	−0.25	−0.14	O9	
19	0 54 24.039	−37 39 17.13	21.42	−0.21	...	B2.5	
FIELD D							
1	0 54 34.625	−37 39 19.70	21.00	0.05	...		composite?
2	0 54 26.406	−37 39 52.05	19.90	0.03	...	A1	Balmer lines somewhat strong
3	0 54 31.848	−37 40 00.89	21.50	0.03	0.12		composite?
4	0 54 23.153	−37 40 46.30	19.85	−0.12	...		H II region
5	0 54 25.597	−37 41 03.44	19.97	−0.05	...	B4	for Gal. abundance; B3 if metal-poor
6	0 54 30.934	−37 41 06.53	20.47	0.00	...	A1	composite?
7	0 54 21.956	−37 41 45.67	20.04	0.14	...	A4	
8	0 54 31.235	−37 41 55.96	19.52	−0.12	...	B1.5	
9	0 54 29.782	−37 42 19.24	21.38	−0.23	...	B1.5	noisy
10	0 54 32.251	−37 42 49.26	19.81	0.11	0.23	A4	
11	0 54 26.794	−37 43 27.02	20.64	−0.24	...		H II region
12	0 54 32.423	−37 43 37.46	18.65	0.17	0.29	A2	Balmer lines filled
13	0 54 26.105	−37 43 56.84	18.98	0.03	0.14	A0	
14	0 54 36.371	−37 44 02.97	19.09	−0.14	−0.17	B3	metal poor, Balmer lines broad
15	0 54 40.048	−37 44 23.12	20.61	−0.11	−0.08	B8	Si II weak: metal deficiency?
16	0 54 32.892	−37 45 02.51	20.92	0.06	0.18	A2–A3	
17	0 54 32.693	−37 45 21.46	19.54	0.02	0.13	B9–A0	
18	0 54 21.804	−37 46 04.60	19.83	−0.01	0.08	B9	metal poor

Table 3. A-8 and D-13: basic properties and stellar parameters

Star	A-8	D-13
Spectral Type	B9–A0 Ia	A0 Ia
RA (J2000)	0 55 41.619	0 54 26.105
DEC (J2000)	−37 40 58.61	−37 43 56.84
v_{rad} (km s ^{−1})	+122	+189
<i>Atmospheric:</i>		
T_{eff} (K)	10000 ± 300	9500 ± 300
log g (cgs)	1.60 ± 0.15	1.35 ± 0.15
ξ (km s ^{−1})	8	8
y (by number)	0.09	0.12
[M/H] (dex)	−0.7 ± 0.2	−0.3 ± 0.2
<i>Photometric:</i>		
V	19.44 ± 0.03	18.98 ± 0.03
$B - V$	−0.01 ± 0.03	0.03 ± 0.03
$E(B - V)$	0.02 ± 0.03	0.03 ± 0.03
M_V	−7.15 ± 0.12	−7.64 ± 0.12
$B.C.^a$	−0.47	−0.41
M_{bol}	−7.62 ± 0.12	−8.05 ± 0.12
<i>Physical:</i>		
log L/L_{\odot}	4.90 ± 0.05	5.08 ± 0.05
R/R_{\odot}	94 ± 8	128 ± 11
$M^{\text{ZAMS}}/M_{\odot}^b$	16 ± 3	19 ± 3
$M^{\text{spec}}/M_{\odot}$	13 ± 2	13 ± 3

^afrom Schmidt-Kaler (1982)

^bfrom comparison with stellar evolution tracks
from Meader & Meynet (2001)

This figure "f1.jpg" is available in "jpg" format from:

<http://arXiv.org/ps/astro-ph/0111070v1>

This figure "f2.jpg" is available in "jpg" format from:

<http://arXiv.org/ps/astro-ph/0111070v1>

This figure "f3.jpg" is available in "jpg" format from:

<http://arXiv.org/ps/astro-ph/0111070v1>

This figure "f4.jpg" is available in "jpg" format from:

<http://arXiv.org/ps/astro-ph/0111070v1>

This figure "f5.jpg" is available in "jpg" format from:

<http://arXiv.org/ps/astro-ph/0111070v1>